JGR Space Physics

RESEARCH ARTICLE
10.1029/2025JA033830

Theory and Modeling of Large Scale Plasmapause Surface Waves

T. Elsden[1], D. J. Southwood[2], O. Allanson[3], M. O. Archer[2], M. D. Hartinger[4,5], and A. N. Wright[1]

[1]School of Mathematics and Statistics, University of St Andrews, St Andrews, UK, [2]Space, Plasma, and Climate Community, Department of Physics, Imperial College London, London, UK, [3]Space Environment and Radio Engineering, School of Engineering, University of Birmingham, Birmingham, UK, [4]Department of Earth, Planetary, and Space Sciences, University of California, Los Angeles, CA, USA, [5]Space Science Institute, Boulder, CO, USA

Key Points:

- We excite a large azimuthal scale surface wave on the plasmapause driven from the magnetopause
- We present a new analytical solution for this surface wave and validate it with magnetohydrodynamic simulations
- For heightened geomagnetic activity, this potentially provides a new mechanism for ultra-low frequency waves to access the inner magnetosphere

Correspondence to:
T. Elsden,
te55@st-andrews.ac.uk

Citation:
Elsden, T., Southwood, D. J., Allanson, O., Archer, M. O., Hartinger, M. D., & Wright, A. N. (2025). Theory and modeling of large scale plasmapause surface waves. *Journal of Geophysical Research: Space Physics*, *130*, e2025JA033830. https://doi.org/10.1029/2025JA033830

Received 7 FEB 2025
Accepted 19 AUG 2025

Author Contributions:
Conceptualization: T. Elsden, D. J. Southwood
Data curation: T. Elsden
Formal analysis: T. Elsden
Investigation: T. Elsden, D. J. Southwood
Methodology: T. Elsden, D. J. Southwood
Project administration: T. Elsden
Software: T. Elsden, A. N. Wright
Supervision: T. Elsden
Validation: T. Elsden, D. J. Southwood, O. Allanson, M. O. Archer, M. D. Hartinger, A. N. Wright
Visualization: T. Elsden, D. J. Southwood
Writing – original draft: T. Elsden, D. J. Southwood, O. Allanson, M. O. Archer, M. D. Hartinger, A. N. Wright
Writing – review & editing: T. Elsden, D. J. Southwood, O. Allanson, M. O. Archer, M. D. Hartinger, A. N. Wright

Abstract The plasmapause in Earth's magnetosphere represents the boundary between the plasma which co-rotates with the Earth (plasmasphere), and the more tenuous plasmatrough outside. The density change across the plasmapause can be large, changing by approximately 1–2 orders of magnitude depending on the prevailing conditions. This would suggest it to be a location where magnetohydrodynamic (MHD) surface waves can form, and indeed, this has been proposed in previous works to explain ultra-low frequency (ULF) wave observations around the plasmapause location. The main question is how such a large scale surface wave on the plasmapause would be excited. In this paper, we propose a model whereby surface waves at the plasmapause are driven by energy input from the magnetopause through solar wind driving. We derive an analytical form for the amplitude of these surface waves with this new driven boundary condition at the magnetopause. The excitation of these waves is then tested in several MHD simulations, where the model geometry, wavenumbers and temporal dependence of the magnetopause driver are varied. We establish that surface waves on the plasmapause can be excited by driving from the magnetopause, and that this still occurs with impulsive and continuous broadband driving. The azimuthal scale of the wave is a critical factor for this excitation, with longer azimuthal scales more favorable for driving larger amplitude surface waves. This mechanism provides new insight for how large scale and large amplitude ULF waves can access the inner magnetosphere, with potential implications for their interaction with radiation belt particles.

Plain Language Summary The space surrounding the Earth dominated by Earth's magnetic field is known as the magnetosphere. This volume extends about 65,000 km from the Earth in the sunward direction in average conditions. Within this medium, there exists a sharp density gradient, known as the plasmapause, where the plasma density can change by 1–2 orders of magnitude. Such a density change forms a surface on which waves can form, much like waves on the surface of water. This study presents a new theory together with computational simulations of how these surface waves inside the magnetosphere can be driven by the solar wind, which bombards the outer surface of the magnetosphere (the magnetopause). The location of these excited surface waves has important implications for the acceleration of particles to high energies in the magnetosphere, which present a hazard for spacecraft and astronauts.

1. Introduction

Magnetohydrodynamic (MHD) surface waves can form at the boundary between two media with different plasma conditions (e.g., magnetic field strength/direction, density, velocity). Such waves have been the subject of extensive study in both solar coronal (Nakariakov et al., 2016; Poedts et al., 1989; Wentzel, 1979) and magnetospheric (Chen & Hasegawa, 1974; Plaschke et al., 2009) contexts. Focusing on Earth's magnetosphere, several authors for example, Plaschke and Glassmeier (2011), Archer et al. (2021, 2024) have shown that surface modes are important in the ultra-low frequency (ULF), Pc5-6, (less than 7 mHz) signals detected in the vicinity of the open-closed boundary (OCB), the boundary between the open field lines of the polar cap and the closed field lines found at lower latitudes. The surface providing the source of these waves is the dayside magnetopause, with the waves driven by buffeting from the pristine solar wind (Takahashi & Ukhorskiy, 2007) and/or dayside transients (Plaschke et al., 2018).

The early work by Chen and Hasegawa (1974) on surface waves in the magnetosphere, suggested that the mode could be excited at the plasmapause, the large plasma density gradient deep within the magnetosphere

(Lemaire, 1974; Lemaire & Gringauz, 1998). In steady state the plasmapause bounds the volume of the magnetosphere, the plasmasphere, where the cold plasma executes closed orbits about the Earth. This region is then separated from the plasmatrough flux tubes at larger L-shells, where flux tubes connect for part of their circulation about the Earth to the solar wind and allow plasma to escape. In recent years, substantive work has been undertaken to statistically model the location and structure of the plasmasphere and its outer boundary under varying conditions (e.g., Del Corpo et al., 2020; Ripoll et al., 2022). In this paper, we will not consider in detail the significant variability of the plasmapause, but note that an important aspect is that the density contrast across the boundary can be substantial (e.g., 1–2 orders of magnitude for the electron density, Carpenter & Anderson, 1992; Gallagher et al., 2000).

The MHD surface wave is characterized by being evanescent (decaying) on both sides of the interface (Plaschke & Glassmeier, 2011). This decay is heavily dependent on the azimuthal wavelength of the surface wave, with longer wavelengths (smaller azimuthal wavenumbers (m)), decaying less steeply. As a fast MHD mode, the surface wave can resonantly couple to Alfvén waves on individual field lines, through field line resonance (FLR) (Southwood, 1974).

The specific motivation for the study of MHD surface waves at the Earth's plasmapause arose from a previous paper, where we modeled numerically the excitation of transverse MHD waves in Saturn's ionosphere (Elsden & Southwood, 2023). The ionosphere was represented by a thin shell of enhanced density with respect to the magnetosphere, where the density gradient at this interface was steep, akin to that at the Earth's plasmapause. Driving fast waves from further out in Saturn's magnetosphere excited distinct FLRs, both in the ionosphere and magnetosphere as well as within the density gradient itself (see Figure 3 of Elsden and Southwood (2023) for reference). It was found that the FLR excited within the density gradient was significantly weaker than the FLRs elsewhere. This results from the FLR amplitude being inversely proportional to the local density gradient across magnetic shells (Wright & Thompson, 1994).

In the previous study, we did not consider the interpretation of a surface mode excitation at the density interface. In Earth's magnetosphere, there have been several previous observations of ULF waves around the plasmapause location attributed to both surface waves (Fukunishi & Lanzerotti, 1974; Lanzerotti et al., 1973; Liu et al., 2011) and FLRs (Fukunishi, 1975). In this article we examine the excitation of a surface mode at the plasmapause as well as the FLRs it excites and suggest it is indeed very relevant to understanding the magnetospheric ULF spectrum. In particular, we explore conditions under which it can be excited by energy from pressure variations buffeting the magnetopause. In these circumstances the mode can be an effective eigenmode of the entire magnetosphere, as posited by Nenovski et al. (2007) and Nenovski (2021). Estimates of the penetration of magnetopause surface waves into the magnetosphere by Archer and Plaschke (2015) suggest a decay length from the nose of the magnetopause of $8.5R_E$ for the fundamental mode. This concept differs from the work of Chen and Hasegawa (1974) who modeled an isolated plasmapause using an initial value problem setup (as opposed to considering the larger magnetosphere with an outer driven boundary). This study aims to elucidate a process by which substantial ULF wave energy can reach deep into the magnetosphere, and therefore play a role in radiation belt wave-particle interactions. We employ both analytical and computational modeling, using a simple MHD box model to examine the structure of plasmapause surface modes.

The paper is structured as follows: Section 2 treats the derivation of an analytical form for the surface wave at the plasmapause with a driven outer boundary condition; Section 3 considers several MHD simulations exploring the validity of the surface mode excitation; Section 4 discusses the results and Section 5 provides a succinct list of the main conclusions; Appendix A provides more details on the analytical form of the surface mode frequency, intended to be a transparent resource for future readers.

2. Surface Modes With a Driven Outer Boundary Condition

In previous works (e.g., Uberoi, 1989; Wentzel, 1979), the surface wave is solved for under the boundary conditions that the wave decays to 0 at large distances either side away from the surface. Taking the surface to be the inner density gradient equivalent to the plasmapause, the surface wave is an eigenmode of the whole cavity, despite evanescing in both directions normal to the surface. In the following analysis, we introduce that the system is driven from the outer (magnetopause) boundary and examine how the signal is structured throughout the cavity. We proceed similarly to the works of Wentzel (1979) and Uberoi (1989), but first introduce the MHD box model used for our analysis.

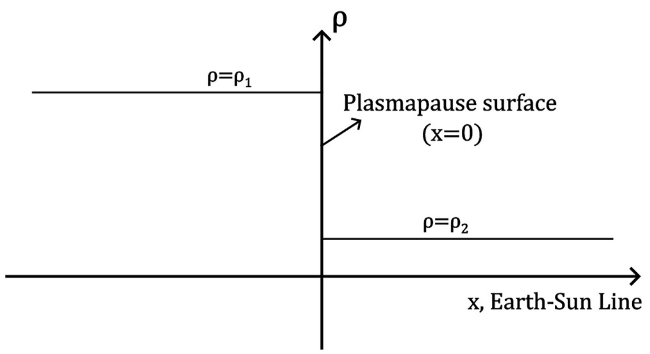

Figure 1. Schematic showing the density $\rho(x)$, indicating two regions of constant but different densities ρ_1 and ρ_2, forming an interface (surface) at $x = 0$, assuming that $\rho_1 > \rho_2$. The background magnetic field is straight, given by $\mathbf{B} = B_0\hat{\mathbf{z}}$.

Consider a cold, low-β plasma, with a straight, uniform background magnetic field $\mathbf{B} = B_0\hat{\mathbf{z}}$. If the plasma is only inhomogeneous in the $\hat{\mathbf{x}}$ direction, we may look for solutions proportional to $e^{i(k_y y + k_z z - \omega t)}$, for azimuthal and field-aligned wavenumbers k_y and k_z, and angular frequency ω. The linear, ideal MHD equations can then be reduced to a single wave equation (in any component, here we choose b_z) as

$$\epsilon(x)\left[\frac{\mathrm{d}^2 b_z}{\mathrm{d}x^2} + \left(\frac{\epsilon(x)}{B_0^2} - k_y^2\right) b_z\right] = \frac{\mathrm{d}\epsilon(x)}{\mathrm{d}x}\frac{\mathrm{d}b_z}{\mathrm{d}x}, \tag{1}$$

where

$$\epsilon(x) = \mu_0 \rho(x)\omega^2 - k_z^2 B_0^2, \tag{2}$$

with $\rho(x)$, the background plasma density and μ_0, the magnetic permeability. Equation 1 is essentially Equation 5 from Uberoi (1989) (however there is a typographical error in their equation, missing multiplication by b_z inside of their large square brackets). Equation 6 of Wentzel (1979) presents an equivalent form of the equations, instead for the plasma displacement ξ_x. The derivative of ϵ with respect to x on the right hand side of Equation 1 is only non-zero if the density varies with x.

Consider the case as shown in Figure 1, such that the density in both regions is constant but different. Then Equation 1 (in each region) reduces to

$$\frac{\mathrm{d}^2 b_z}{\mathrm{d}x^2} + \left(\frac{\epsilon}{B_0^2} - k_y^2\right) b_z = 0. \tag{3}$$

This is simply a second order ordinary differential equation with constant coefficients, to be solved in each of the regions. Let the density in region 1, for $x < 0$ be ρ_1, with region 2 for $x > 0$, ρ_2. Then the general solution in each region is

$$b_{z1} = C_1 e^{K_1 x} + D_1 e^{-K_1 x}, \tag{4}$$

$$b_{z2} = C_2 e^{K_2 x} + D_2 e^{-K_2 x}, \tag{5}$$

where

$$K_1 = \sqrt{k_y^2 - \frac{\epsilon_1}{B_0^2}}, \tag{6}$$

$$K_2 = \sqrt{k_y^2 - \frac{\epsilon_2}{B_0^2}}, \tag{7}$$

following the notation of Uberoi (1989), where ϵ_1 and ϵ_2 are determined by evaluating Equation 2 with ρ_1 and ρ_2 respectively. Note that there is a requirement on K_1 and K_2 to be real to enforce exponential not oscillatory solutions for the surface mode. The boundary conditions to be enforced are as follows:

1. $b_{z1} \to 0$ as $x \to -\infty$ (decay of region 1 surface mode).
2. $b_{z2} = b_{z0}(t)$ at $x = x_m$ (driven, time dependent magnetopause boundary value).
3. $\xi_{x1}|_{x=0^-} = \xi_{x2}|_{x=0^+}$ (continuous normal displacement at surface).
4. $b_{z1}|_{x=0^-} = b_{z2}|_{x=0^+}$ (continuous b_z (magnetic pressure) at surface).

Condition 1 immediately implies that $D_1 = 0$ (since $x < 0$ in region 1). Condition 4 in Equations 4 and 5 gives

$$C_1 = C_2 + D_2. \tag{8}$$

Condition 3 can be rewritten as a condition involving b_z using

$$\xi_x = \frac{B_0}{\epsilon}\frac{\mathrm{d}b_z}{\mathrm{d}x}, \tag{9}$$

which can be derived directly from the linear MHD equations (see also Equation 8 of Uberoi (1989)). Then condition 3 becomes

$$\begin{aligned} \xi_{x1}|_{x=0^-} &= \xi_{x2}|_{x=0^+}, \\ \Rightarrow \frac{1}{\epsilon_1}\frac{\mathrm{d}b_{z1}}{\mathrm{d}x}|_{x=0^-} &= \frac{1}{\epsilon_2}\frac{\mathrm{d}b_{z2}}{\mathrm{d}x}|_{x=0^+}, \end{aligned} \tag{10}$$

The derivatives can be written as (using Equations 4 and 5)

$$\begin{aligned} \frac{\mathrm{d}b_{z1}}{\mathrm{d}x} &= C_1K_1e^{K_1x}, \\ \frac{\mathrm{d}b_{z2}}{\mathrm{d}x} &= C_2K_2e^{K_2x} - D_2K_2e^{-K_2x}. \end{aligned}$$

Hence condition 3 becomes

$$\frac{C_1K_1}{\epsilon_1} = \frac{C_2K_2 - D_2K_2}{\epsilon_2}. \tag{11}$$

Finally, condition 2, which represents the driven outer boundary condition can be written as

$$b_{z0} = C_2e^{K_2x_m} + D_2e^{-K_2x_m}, \tag{12}$$

which follows from Equation 5 with $x = x_m$ and assuming that the time dependence of the boundary driver is proportional to $e^{i\omega t}$ as assumed for the overall surface mode.

Equations 8, 11, and 12 give three equations for three unknowns C_1, C_2, D_2. Eliminate C_1 in Equation 11 using Equation 8 to give

$$\frac{(C_2 + D_2)K_1}{\epsilon_1} = \frac{(C_2 - D_2)K_2}{\epsilon_2}. \tag{13}$$

Now D_2 can be replaced in terms of C_2 by rearranging Equation 12 as

$$D_2 = b_{z0}e^{K_2x_m} - C_2e^{2K_2x_m}. \tag{14}$$

Substituting this back into Equation 13 (after 5–6 lines of algebra) gives

$$C_2 = \frac{b_{z0}e^{K_2x_m}(K_1 + K_2r)}{K_2r(1 + e^{2K_2x_m}) - K_1(1 - e^{2K_2x_m})}, \tag{15}$$

where

$$r = \epsilon_1/\epsilon_2, \tag{16}$$

a factor introduced also by Wentzel (1979) to help tidy up the algebra. Dividing through by the exponential term allows for a re-expression in terms of hyperbolic functions as

$$C_2 = \frac{b_{z0}}{2}\left\{\frac{K_1 + K_2 r}{K_1 \sinh(K_2 x_m) + K_2 r \cosh(K_2 x_m)}\right\}. \tag{17}$$

This can then be substituted back into Equation 14 to give the form for D_2 as

$$D_2 = \frac{b_{z0}}{2}\left\{\frac{K_2 r - K_1}{K_1 \sinh(K_2 x_m) + K_2 r \cosh(K_2 x_m)}\right\}.$$

It can be quickly checked that the boundary condition 2 is satisfied by these coefficients as

$$\begin{aligned}
b_{z2}(x = x_m) =\ & C_2 e^{K_2 x_m} + D_2 e^{-K_2 x_m}, \\
=\ & \frac{b_{z0}}{2}\left\{\frac{(K_1 + K_2 r)\, e^{K_2 x_m}}{K_1 \sinh(K_2 x_m) + K_2 r \cosh(K_2 x_m)} + \frac{(K_2 r - K_1)\, e^{-K_2 x_m}}{K_1 \sinh(K_2 x_m) + K_2 r \cosh(K_2 x_m)}\right\}, \\
=\ & \frac{b_{z0}}{2}\left\{\frac{K_1\left(e^{K_2 x_m} - e^{-K_2 x_m}\right) + K_2 r\left(e^{K_2 x_m} + e^{-K_2 x_m}\right)}{K_1 \sinh(K_2 x_m) + K_2 r \cosh(K_2 x_m)}\right\}, \\
=\ & \frac{b_{z0}}{2}\left\{\frac{2K_1 \sinh(K_2 x_m) + 2K_2 r \cosh(K_2 x_m)}{K_1 \sinh(K_2 x_m) + K_2 r \cosh(K_2 x_m)}\right\}, \\
=\ & b_{z0}.
\end{aligned}$$

The coefficient C_1 is found simply from Equation 8 as

$$C_1 = C_2 + D_2 = \frac{b_{z0} K_2 r}{K_1 \sinh(K_2 x_m) + K_2 r \cosh(K_2 x_m)}.$$

Hence the solutions in the two regions become

$$b_{z1} = C_1 e^{K_1 x} = \frac{b_{z0} K_2 r}{K_1 \sinh(K_2 x_m) + K_2 r \cosh(K_2 x_m)} e^{K_1 x}, \tag{18}$$

$$\begin{aligned}
b_{z2} =\ & C_2 e^{K_2 x} + D_2 e^{-K_2 x}, \\
=\ & b_{z0}\left\{\frac{K_1 \sinh(K_2 x) + K_2 r \cosh(K_2 x)}{K_1 \sinh(K_2 x_m) + K_2 r \cosh(K_2 x_m)}\right\}.
\end{aligned} \tag{19}$$

There are a few notes of interest about the form of these solutions. Both of the solutions scale approximately as $e^{-K_2 x_m}$ through the term in the denominator (given the exponential form of sinh and cosh and assuming $x_m > 0$, for x_m the magnetopause position), implying that the amplitude is generally lower the further away that the magnetopause is, as perhaps expected. However, this will obviously depend on the level of evanescence defined by the effective exponential decay length in x, $1/K_2$, in region 2. In the inner region (region 1), the behavior is that of a decaying exponential as per the classical solution ($\sim e^{K_1 x}$ for $x < 0$). In region 2, there is a balance of exponentials for matching the driven boundary condition and the conditions of the surface.

2.1. Surface Mode Frequency

In previous works (e.g., Chen & Hasegawa, 1974; Plaschke & Glassmeier, 2011; Uberoi, 1989; Wentzel, 1979), making an assumption such as incompressibility or $k_y \gg k_z$ permits an explicit dispersion relation to be derived for the surface mode frequency. However, without these assumptions, and including the extra term retained through the new outer boundary condition here seems to preclude such a form. We can take a numerical approach in the first instance, by simply plotting the form of the solution given by Equations 18 and 19 for different frequencies, and determining which frequency maximizes the amplitude at the surface. This approach has been previously used to determine natural fast cavity mode frequencies in simulations by Wright and Rickard (1995). Recall that the frequency enters into Equations 18 and 19 through K_1 and K_2, which depend upon ϵ_1 and ϵ_2 respectively, which depend on the frequency (Equation 2).

10.1029/2025JA033830

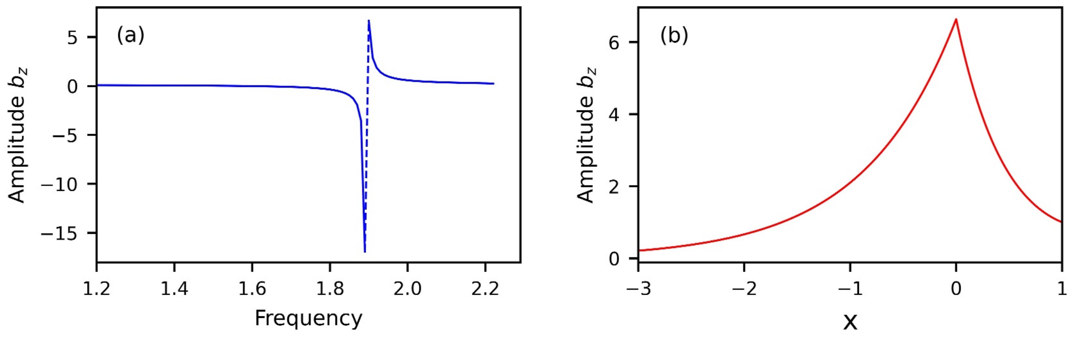

Figure 2. (a) Amplitude at $x = 0$ of the surface mode for different driving frequencies. The dashed blue line is purely illustrative to connect the positive and negative amplitude solutions across the resonant frequency (where the amplitude tends to infinity). (b) b_z from Equations 18 and 19 for frequency $\omega = 1.90$ (exact solution is $\omega = 1.8928$).

Consider the following model for testing of the above analytical derivations: a Cartesian box with dimensions (in dimensionless units) $x : [-3, 1]$, $y : [-1, 1]$, $z : [-1, 1]$, such that for a fundamental mode in y and z with perfectly reflecting boundary conditions, $k_y = k_z = \pi/2$ (half wavelength fundamental modes); the plasma density in the inner region is 10 times that of the outer region, such that $\rho_1 = 1$ and $\rho_2 = 0.1$, in a dimensionless regime with density normalized by that of the inner region; the density surface lies at $x = 0$. Using a bisection approach to maximize the amplitude, we find a surface mode frequency of $\omega = 1.8928$ to 4 decimal places, as shown in Figure 2a, where the amplitude at the surface is plotted against frequency. The amplitude at the surface becomes infinite in the analytical form for b_z when using the exact frequency. Hence, if a smaller step size in frequency were plotted, the amplitude would be larger.

Figure 2b displays the spatial structure of the mode by plotting $b_z(x)$ from Equations 18 and 19 on either side of the surface for the frequency $\omega = 1.90$. It is chosen to plot a slightly off-resonant frequency so that the amplitude at the surface is relatively small such that the driven boundary value (of $b_{z0} = 1$ here) is visible. The spatial structure is very clear and typical of what is envisaged for a surface mode, peaking at the surface at $x = 0$, and decaying away from the surface toward the inner/outer boundary. From a magnetospheric perspective, the implication is that near the OCB magnetic shells the amplitude would evanesce as one moves to lower L shells. However, at some point in the trough volume the evanescence ceases and the wave amplitude grows to peak at the plasmapause boundary. The evanescence away from the driven boundary is not particularly evident in Figure 2b, due to the very large amplitude at the surface and close proximity of the driven boundary ($x = 1$) to the surface ($x = 0$), though this will become more apparent in later figures. On magnetic shells inside the plasmasphere the amplitude again evanesces as one moves toward Earth. In the case shown where the density is discontinuous at the surface, the derivative $\mathrm{d}b_z/\mathrm{d}x$ is discontinuous also, resulting in a sharp kink at the surface. This can be thought of as coming from Equation 10, with ϵ_1 and ϵ_2 having different signs (see discussion preceding Equation 10 of Wentzel (1979) for more information).

Searching for a frequency which maximizes the amplitude of the surface gives a "numerical" way of finding the surface mode natural frequency. It is clearly of interest as to how this compares to the frequencies found without the driven boundary condition. In Appendix A, we follow the derivation of the dispersion relation of Wentzel (1979), and show by extension of their work how the resulting dispersion relation can be solved analytically. It is then demonstrated that the frequencies predicted analytically for the classical surface wave are very close to those found "numerically" by the above maximization of the amplitude process with the driven boundary condition. However, there is a difference between them, when the driven boundary is taken to be "close" to the density surface. Fundamentally, this difference depends on the penetration of the mode from the driven boundary to the density surface. Around the subsolar point, the azimuthal wavenumber can be very small, and with long field line lengths here (small field-aligned wavenumber), the penetration from the driven boundary could be significant. This would require further investigation in a geometrically more accurate magnetospheric model.

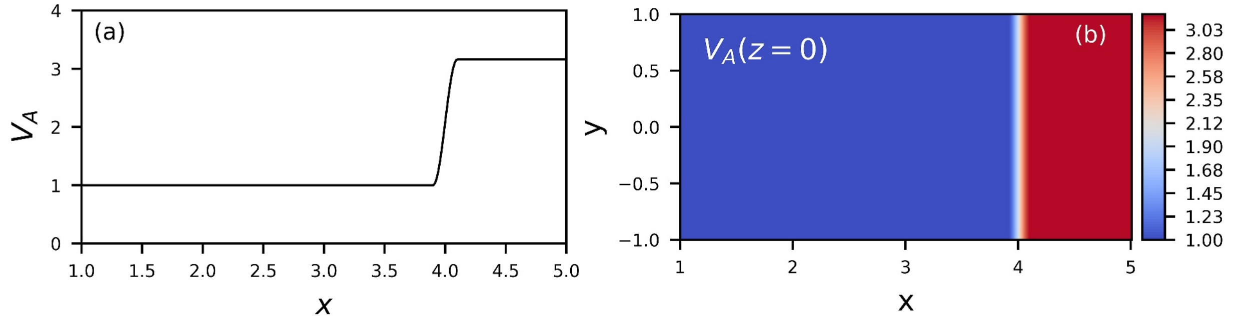

Figure 3. (a) Alfvén speed as a function of x at $y = z = 0$ (b) Contour of the Alfvén speed in the equatorial ($z = 0$) plane.

3. Numerical Modeling

The analytical formulas and ideas above can now be compared against MHD simulations, and the efficacy of driving from the outer boundary can be further explored. We use the numerical model of Wright and Elsden (2020), which solves the linear MHD equations for a cold plasma. In this paper, we use a Cartesian box geometry as a means to determine the fundamental physics of the problem. Furthermore it appears that, to the best of our knowledge, no such simplified simulations of surface waves exist in the literature. Future studies will consider the more realistic dipolar magnetic field geometry. Several simulation runs are presented in this section, with the aim of beginning with the simplest possible setup to lay the groundwork for more sophisticated runs toward the end of the section. Section 3.1 considers a small box model to validate the analytical theory and concepts; Section 3.2 expands the size of the domain to provide a better magnetospheric comparison; Sections 3.3 and 3.4 explore impulsive and broadband external driving sources respectively.

3.1. Small Cartesian Box

We begin with a test model geometry, employing a small Cartesian box of normalized dimensions $x : [1, 5]$, $y : [-1, 1]$, $z : [0, 1]$, which is essentially equivalent to the example from the previous section with a translated x coordinate. Throughout the paper, we quote results in normalized quantities. This is due to the simplified model setup used (e.g., constant density regions and straight background magnetic field) and it is felt that comparative amplitudes for example, between the driven boundary and the surface, illustrate the excitation mechanism clearly enough.

A symmetry condition is applied at $z = 0$ such that we only need to consider the upper half of the field line (this enforces odd harmonics along the field in terms of the perpendicular components of the magnetic field perturbation). Figure 3a displays the x dependence of the Alfvén speed, with panel (b) displaying the Alfvén speed as a contour plot in the equatorial ($z = 0$) plane. The values for V_A come from taking $\rho_1 = 1$ in the region $x < 3.9$, and $\rho_2 = 0.1$ in the region $x > 4.1$. The resulting Alfvén speed is chosen to vary smoothly over $3.9 < x < 4.1$ (using a sinusoidal function), for numerical stability, rather than a discontinuity as modeled analytically. It is important to properly resolve the change in the Alfvén speed, and hence the number of grid points for each direction (x, y, z) is taken as (300, 50, 25). Only enough grid points to resolve a half wavelength are required in the y and z directions. The other boundary conditions (besides at $z = 0$) are reflecting at $x = 1$, $y = \pm 1$, $z = 1$. This gives, for fundamental modes, $k_y = \pi/2$, $k_z = \pi/2$. A dimensionless uniform value for the magnetic diffusivity of $\eta = 0.0005$ is taken to introduce a small amount of dissipation into the system, to prevent phase mixing below the grid scale.

The outer boundary at $x = 5$ is driven monochromatically with perturbations to b_z (mimicking magnetic pressure disturbances) at the frequency found from the previous analysis, $\omega_{surf} = 1.8928$ (period $\tau_{surf} = 2\pi/\omega_{surf} = 3.3195$). Despite being chosen for testing and simplicity, such monochromatic driving could result from periodic density structures in the solar wind impacting the magnetopause (Di Matteo et al., 2022). The azimuthal variation of the driver is chosen such that b_z has a node (zero) at $y = 0$ and maxima/minima at $y = \pm 1$, to enforce $k_y = \pi/2$. This structure has the advantage of exciting a mode exactly with this azimuthal structure, that is, a single value of k_y, providing a better comparison with the theory. In testing, it was found that using a

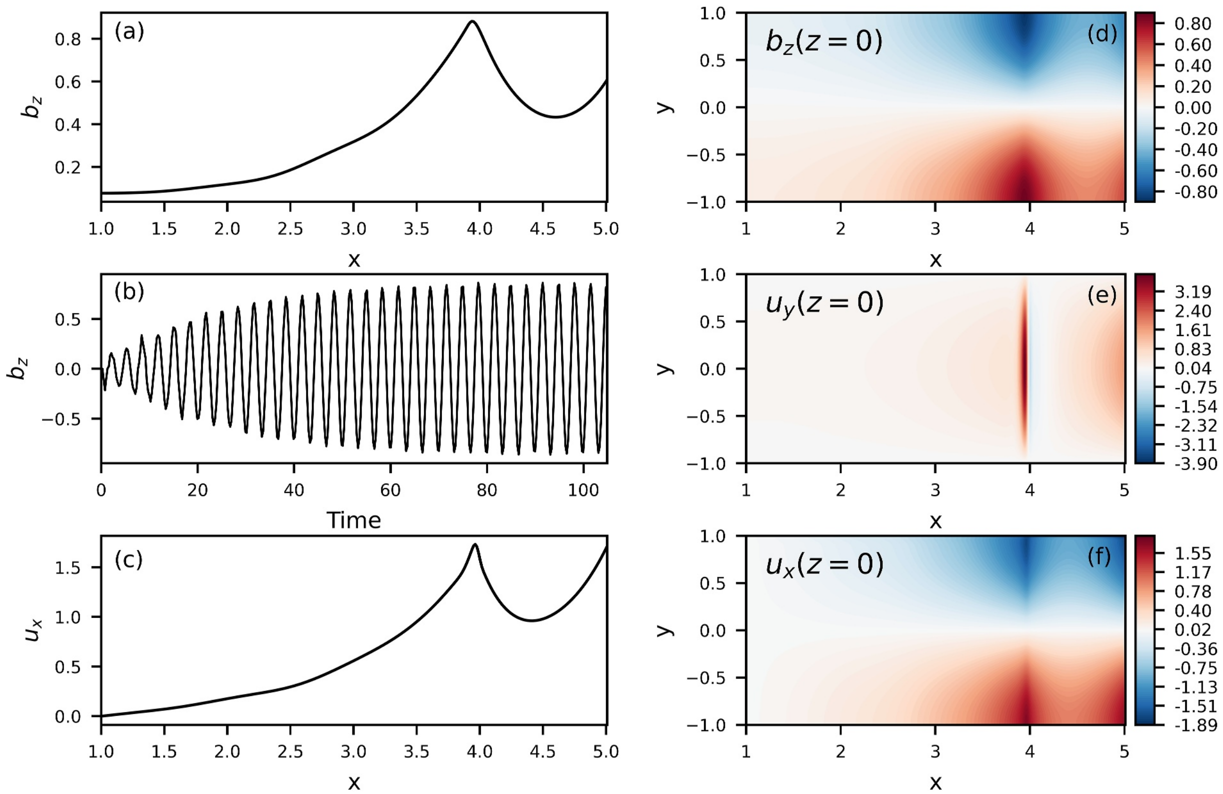

Figure 4. Results from the small Cartesian box simulation. (a) b_z as a function of x at $y = -1$ (lower y boundary) at a late simulation time, $t = 104.92$. (b) Time series of b_z at the surface at $x = 4.0$, $y = -1.0$. (c) Velocity component u_x at a slightly different time to panel (a) ($t = 97.05$), when u_x has a maximum at the surface, also at $y = -1$. (d) Contour plot of b_z in the $z = 0$ plane at the same time as (a), showing the global surface wave structure. (e) Contour plot of u_y in the $z = 0$ plane at a late time, giving the field line resonance response. (f) Contour plot of u_x in the $z = 0$ plane at the same time as (c).

driver symmetric in azimuth excited $k_y = 0$ modes as well as the desired $k_y = \pi/2$ modes for the given boundary conditions.

Figure 4a shows the variation of $b_z(x)$ at a time of a maximum of the surface mode amplitude. It can be clearly seen there is a distinct peak in the amplitude at the surface, with evanescent behavior on either side, in close agreement with the structure predicted by the analytical formulas. Figure 4b displays a time series of b_z at $(x, y, z) = (4, -1, 0)$, that is, at the surface and at a y-location where b_z has a maximum. The resonant growth is clear, which plateaus at around $t = 80$ due to dissipation provided through resistivity (see later description of panel (e)). A contour plot in the equatorial plane of $b_z(x, y, z = 0)$ is given in Figure 4d, taken at the same time as the line plot in panel (a). This shows the global nature of the surface wave, as well as clearly depicting the structure in the $\hat{\mathbf{x}}$ and $\hat{\mathbf{y}}$ directions. The global surface wave is driving a field line resonance (FLR), which results in strong azimuthal velocity (u_y) perturbations in the density surface, shown as a contour plot in Figure 4e. It is in the density gradient that the local Alfvén frequency matches the surface wave frequency. Energy from the surface wave is pumped into the FLR, which saturates in amplitude once losses through resistivity balance energy fed into the system through the driven boundary. The FLR is driven by azimuthal gradients in the surface (fast) wave (Wright, 1994), and hence the strongest response in u_y is around $y = 0$ where $\partial b_z/\partial y$ is largest. Figures 4c and 4f display u_x as a function of x and as a contour plot respectively, at a late simulation time (slightly different to panel (a)). This plot is included to indicate that the surface wave, being a fast MHD wave, carries a significant radial velocity component. This corresponds to an azimuthal electric field, which should be important for drift-resonant interactions with particles. This concept is continued in the discussion section. Overall, this model geometry has clearly shown how an interior surface wave (e.g., on the plasmapause) can be driven from an outer boundary (e.g., the magnetopause) and indeed that the frequency predicted from the analytical theory is accurate. With this established, we move to consider a larger simulation domain.

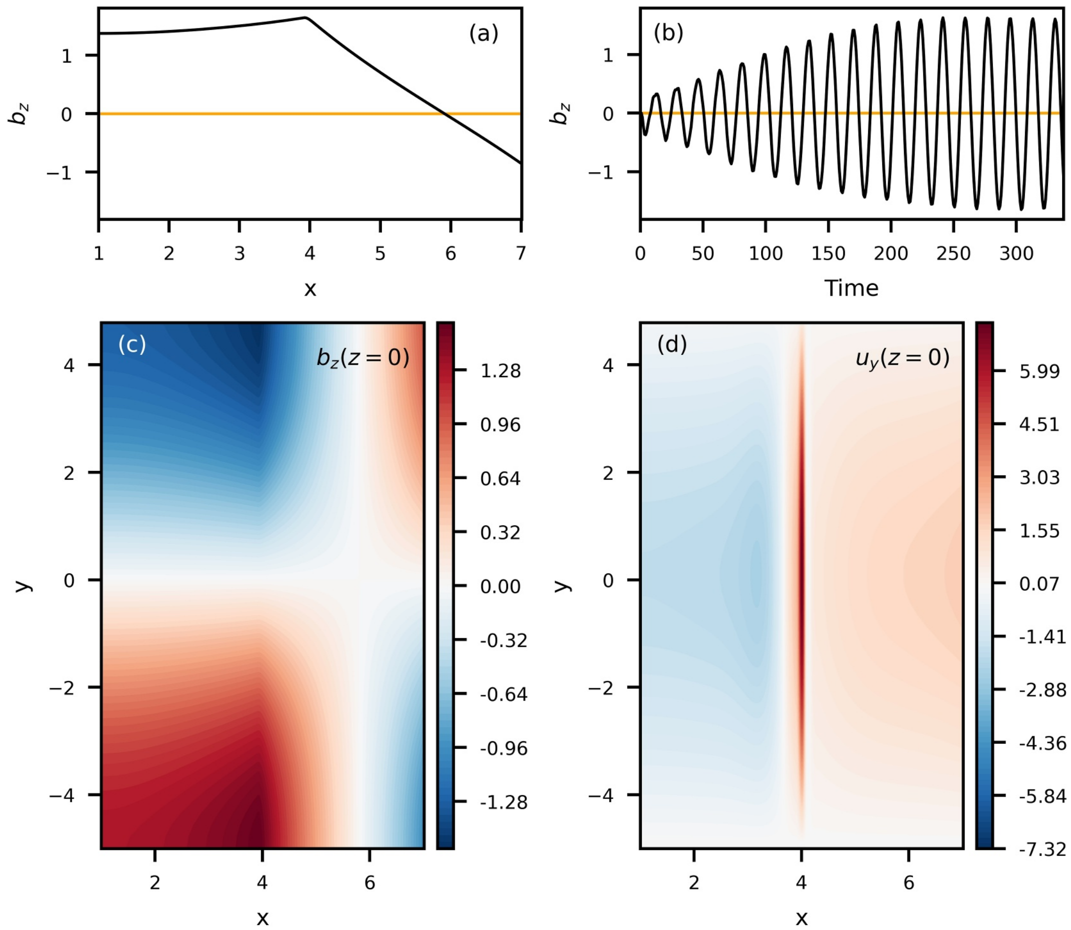

Figure 5. Simulation results from the larger box run. (a) $b_z(x)$ at a late time ($t = 330.90$), at $y = -5$ (lower y boundary). (b) Time series of b_z at the surface at $x = 4$, $y = -5$. (c) Contour plot of b_z in the $z = 0$ plane showing the global surface mode spatial structure, taken at the same time as (a). (d) Contour plot of u_y in the $z = 0$ plane at time $t = 330.90$ showing the field line resonance response.

3.2. Larger Cartesian Box

To model a potentially more realistic magnetospheric scenario, consider the domain given by $x : [1,7]$, $y : [-5,5]$, $z : [0,5]$. If these values were taken to be Earth radii, then this would still be a small version of the true dayside magnetosphere (without any azimuthal curvature). The reason that we have taken a slightly smaller domain azimuthally is due to a restriction enforced by the Cartesian box model with constant Alfvén speed regions. In the inner region, where $V_A = 1$, every field line has the same Alfvén frequency. When k_y is small, the surface mode frequency becomes quite close to the Alfvén frequency of these inner region field lines. Hence, when driving at the surface mode frequency, a significant Alfvén resonance is excited on *every* field line of the inner region. This would of course not occur in a dipole model, where the changing field line length and field strength precludes this coherent response. Therefore, taking a slightly smaller azimuthal extent increases k_y sufficiently to separate the surface and Alfvén resonant frequencies.

The Alfvén speed profile is unchanged from Figure 3 in that the density surface is placed at $x = 4$, but with the outer boundary now at $x = 7$. This is intended to represent a more realistic scenario regarding the distance between the magnetopause and plasmapause (though is still on the small side for quiet conditions). Recall that the analytical solution predicts a dependence of the surface wave amplitude of e^{-x_m} (x_m the magnetopause location), so it is important to see how moving the driven boundary further back affects the wave amplitude. The choice of the extent in each direction yields wavenumbers for fundamental modes in y and z as $k_y = \pi/10$ and $k_z = \pi/10$. The surface mode frequency is found to be $\omega_{surf} = 0.348$ from the numerical approach in Section 2.1, while the

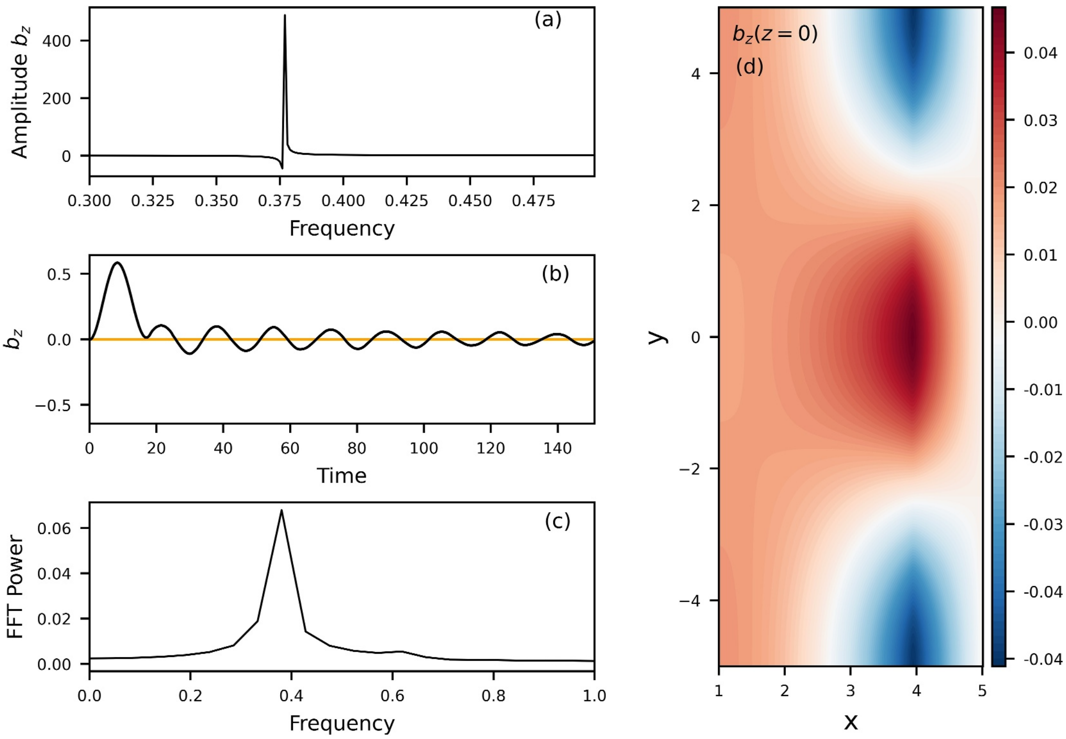

Figure 6. Simulation results from driving with a symmetric impulse of a full wavelength in azimuth. (a) Using the analytic form for b_z and finding the frequency by scanning through ω to see which maximizes the amplitude at the surface ($\omega = 0.377$). (b) $b_z(t)$ at $(x, y) = (4, 0)$ at the surface, showing clearly a particular frequency of oscillation of the surface. (c) Fast Fourier transform (FFT) of time series in (b), with a peak around the predicted angular frequency of $\omega \sim 0.375$ from (a) (within resolution of the FFT). (d) Contour plot of b_z at $t = 139.68$ showing the mode structure of a full wavelength in azimuth.

Alfvén frequency of field lines in the inner region is $\omega_A = k_z V_A = \pi/10 = 0.314$. The magnetic diffusivity is again uniform with value $\eta = 0.0005$.

Figure 5 displays the results from this simulation in a similar format to Figure 4. Panel (a) shows $b_z(x)$ at a late time in the simulation. It is clear that in comparison with Figure 4a, there is far less evanescence of the mode in the x direction. This is also clear from a contour plot of the spatial structure in the $z = 0$ plane shown in panel (c) (taken at the same time), where the decay away from the surface is much less pronounced than the previous simulation. This is due to the much smaller value of k_y used, as expected from classical ULF wave theory (Kivelson & Southwood, 1986; Wright, 1994). Also of note is the reversal of b_z (crossing zero amplitude) around $x = 6$. The time series of $b_z(x = 4)$, at the surface, is given in panel (b), showing again a clear resonant excitation until saturation, further validating the analytical prediction for the frequency. Panel (d) displays the FLR response through a contour plot of u_y at a late simulation time. There is a clear global component to this as well, which contains the azimuthal velocity component of the fast surface wave.

3.3. Impulse Driven

In this simulation, we consider driving impulsively and symmetrically in azimuth to test that the surface mode can still be excited in this way. A domain size of $x : [1, 5]$, $y : [-5, 5]$, $z : [0, 5]$ is used, again with the same change in the densities resulting in the Alfvén speed profile of Figure 3. The shorter domain size in the x-direction, as in Figure 4, is chosen to provide the simplest setup in which to test the impulse excitation of the surface wave. The symmetric nature of the driver about $y = 0$ gives an impulse with a profile which is clearly apparent from the resulting b_z perturbation in the $z = 0$ plane, shown in Figure 6d. This full wavelength in azimuth results in an azimuthal wavenumber of $k_y = \pi/5$. Using this value, the frequency of the surface wave can be determined as before, by using the analytical form for b_z (Equations 18 and 19) and finding which frequency maximizes the amplitude at the surface at $x = 4$. This is shown in Figure 6a, providing a frequency of $\omega = 0.377$. The response

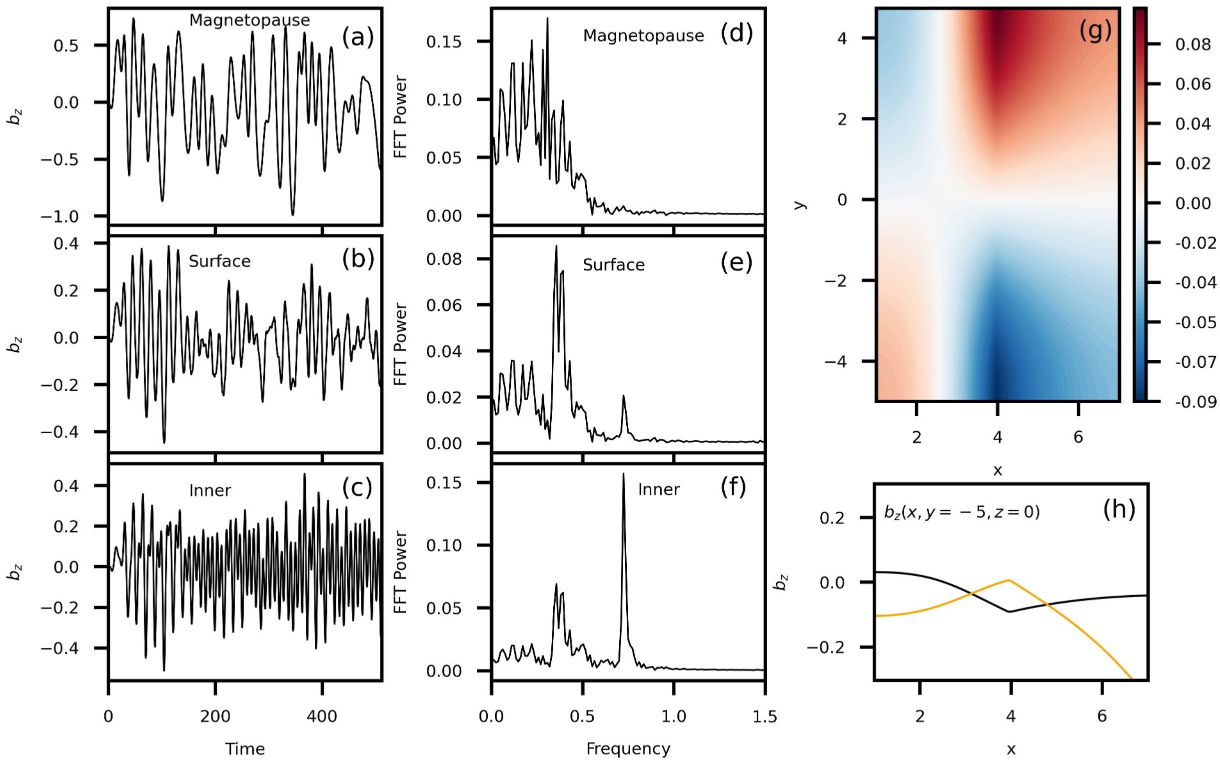

Figure 7. Broadband simulation run with $k_y = \pi/10$. (a–c) Time series of b_z at $y = -5$ (lower boundary) at three different x values: (a) at the driven boundary $x = 7$; (b) at the surface $x = 4$; (c) in the inner region at $x = 1.76$. (d–f) Fast Fourier transforms of the time series in (a–c). (g) Contour plot of b_z at $z = 0$ at a late simulation time ($t = 495.3$). (h) $b_z(x)$ at two different times in the wave period; $t = 495.3$ (black) and $t = 502.6$ (orange).

of b_z at the surface at $x = 4$, $y = 0$ is given in panel (b). The initial positive impulse is indicative of the driving impulse (which has a $\sim \sin^2(\pi t/t_d)$ dependence and a duration of $t_d = 18$), which then settles down to a clearly defined frequency, albeit of smaller amplitude. Taking a fast Fourier transform (FFT) of this time series discarding the initial positive impulse, shown in Figure 6c, gives a very well defined frequency peak at the expected surface mode frequency.

Figure 6d shows the b_z perturbation in the $z = 0$ plane at a late simulation time, clearly displaying the excitation at the surface ($x = 4$). The mode is then evanescent in the direction toward the inner (left) boundary. Another note of interest here is the overlap of the impulse duration with the surface mode frequency. An impulse itself excites a broad range of frequencies, however there must still be a favorable overlap between such frequencies and the desired mode (e.g., surface mode) for efficient energy transfer between them. In this case, the impulse duration of $t = 18$ is close to the surface mode period of $2\pi/0.377 = 16.66$.

3.4. Broadband Continuous Driving

A further type of driving, far more representative of fluctuations of the magnetopause by solar wind dynamic pressure changes, is continuous broadband driving. In this section, we discuss results from two simulations, which differ only by the azimuthal wavenumber k_y of the driving stimulus.

Figure 7 displays results from a simulation where $k_y = \pi/10$, with the identical model geometry as for Figure 5, again using the same Alfvén speed profile from Figure 3, extended to $x = 7$ with the density surface at $x = 4$. Figure 7a shows the time series of b_z at the outer boundary at $x = 7$, giving the time dependence of the driving. Figure 7d plots the FFT of this time series, showing that the signal is made up of a range of frequencies spanning approximately $\omega \in (0, 0.5)$. Figure 7b gives the time series of b_z at the density surface at $x = 4$, with the corresponding FFT in Figure 7e. The FFT reveals that the cavity has filtered the incoming driving signal, with a peak at frequencies between $\omega \sim 0.35$ and $\omega \sim 0.4$ and a higher frequency peak at $\omega \sim 0.72$. This kind of filtering of a broadband driven spectrum by an MHD cavity to reveal natural fast frequencies (though not surface modes) was shown by Wright and Rickard (1995). Figure 7c plots $b_z(t)$ deep into the inner region at $x = 1.76$, with the FFT of this signal given in Figure 7f. The same frequency peaks are visible as in panel (e), but with a much stronger response at the higher frequency. The lower peak frequency is close to the expected surface mode frequency ($\omega = 0.348$). The higher frequency appears to be a cavity resonance of the inner cavity, formed between the inner boundary at $x = 1$ and the density surface at $x = 4$. Figure 7g displays a contour plot of b_z at a time close to a maximum amplitude at the surface, again showing a clear surface mode structure. Panel (h) plots $b_z(x)$ at $y = -5$, $z = 0$ at two different times: the black line is at the same time as the contour plot in panel (g), while the orange line is at a slightly later time. Since there are competing fast waves (surface and cavity modes), it is difficult to define the orange line as at a certain time in a wave period, but it is included to show how the spatial structure of the waves present varies. This combination of cavity and surface waves may lead to potential observational difficulties in terms of associating magnetic compressions at the plasmapause with each mode. Furthermore, the broadband nature of the signal imposed on the boundary at $x = 7$ changes the amplitude there, irrespective of the structure at other locations.

Since the Alfvén speed is uniform in the inner region, we could estimate the frequency for a cavity resonance there using the fast mode dispersion relation in a uniform medium, were the local wavelength in x to be known. Equally, we could use the frequency from the FFT in Figure 7f to confirm the quarter wavelength structure apparent in Figure 7h, between $x = 1$ and $x = 4$. Using the frequency estimate of $\omega = 0.72$ from Figure 7f, together with the wavenumbers in y and z yields

$$\begin{aligned} k_x^2 &= \omega^2 - k_y^2 - k_z^2, \\ &= 0.72^2 - \left(\frac{\pi}{10}\right)^2 - \left(\frac{\pi}{10}\right)^2, \\ \Rightarrow k_x &= 0.567. \end{aligned}$$

Assuming a cavity of width 3 in x (from $x = 1$ to $x = 4$), a quarter wavelength in x would imply $k_x = 2\pi/12 = 0.523$, which is close to the above estimate. This is improved by taking a slightly smaller cavity since the density change starts at $x = 3.9$, which would give an estimated wavelength of $k_x = 0.542$. Further, we may expect the estimate not to be exact since the Alfvén speed jumps from 1 to a finite (rather than infinite) value ($\sqrt{10}$). A very interesting aspect of the estimate is that it suggests the surface acts as an antinode (maximum) of displacement/velocity and a node of b_z for these inner cavity modes. This is further confirmed by plots of the velocity dependence on x, $(u_x(x))$, not given here. Another intriguing point is the efficacy of the excitation of the inner cavity mode, despite the driving frequency not significantly overlapping with this cavity frequency. This potentially points to a more efficient excitation than the surface wave, though this would have to be tested systematically with further simulations and could be something exaggerated by the Cartesian model setup. Indeed, the cavity frequency does not overlap with the Alfvén frequency of the inner region field lines, and hence there is no sink for this trapped energy, which would not occur in a dipole model with varying field line lengths. Overall, this simulation has achieved its aims of showing that the surface wave can still be excited by broadband driving.

Figure 8 also considers a broadband driven system, except with $k_y = \pi/5$, halving the azimuthal extent of the domain. The results are presented similarly to Figure 7. Panels (a)–(c) give time series of b_z at the outer boundary ($x = 7$), at the density surface ($x = 4$) and in the inner region ($x = 1.76$) respectively. Panels (d)–(f) are the corresponding FFTs of these time series. The increased azimuthal wavenumber has decreased the excitation of the inner cavity mode, presumably due to the greater evanescence in the x direction this entails. This is noticeable through a lack of a peak at a higher frequency in panel (e), and that the surface mode frequency peak is larger than the higher frequency peak in panel (f) (compare to the same panels in Figure 7). Panels (g) and (h) display contour plots of b_z at different times, emphasizing the peak at the surface in (g), and the peak at the boundary in (h), showing how the time dependence impacts the mode structure. The dependence of b_z as a function of x for these same times is shown in panel (i), with similar conclusions as the corresponding panel in Figure 7.

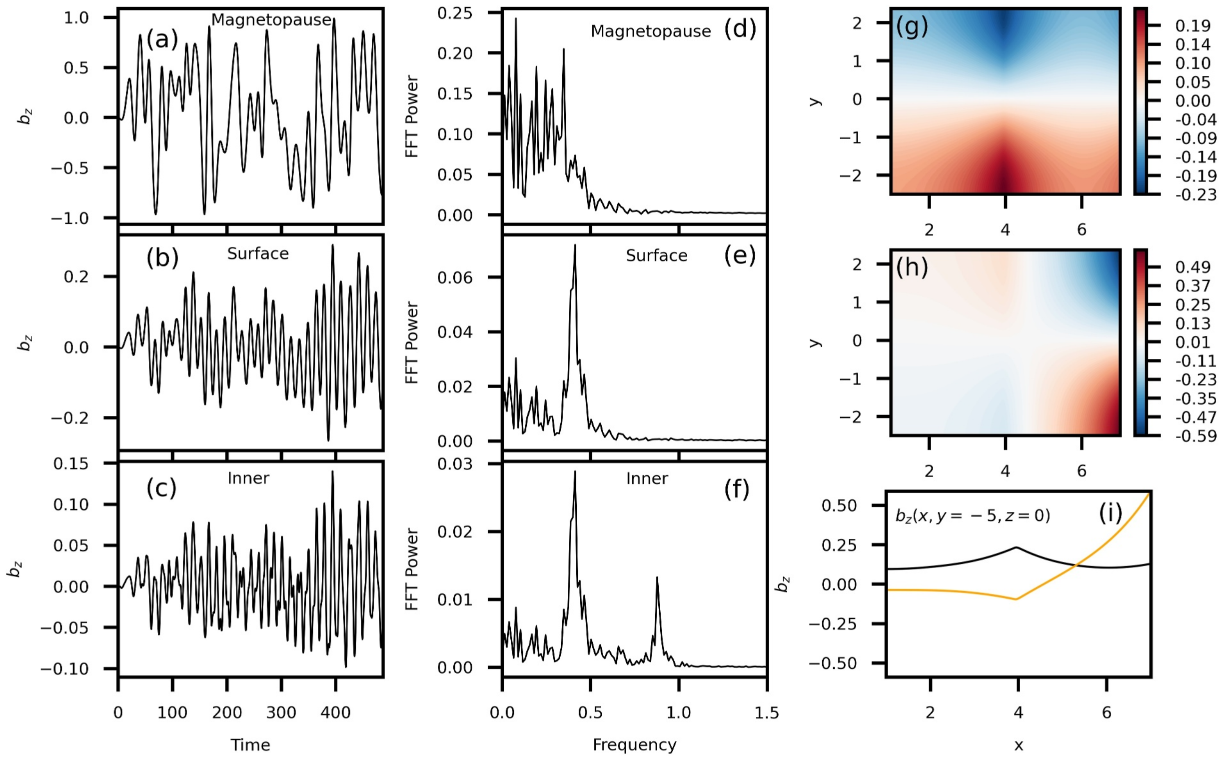

Figure 8. Broadband simulation run with $k_y = \pi/5$. (a)–(c) Time series of b_z at $y = -2.5$ (lower boundary) at three different x values: (a) at the driven boundary $x = 7$; (b) at the surface $x = 4$; (c) in the inner region at $x = 1.76$. (d)–(f) Fast Fourier transforms of the time series in (a)–(c). (g)–(h) Contour plots of b_z at $z = 0$ at a late simulation time, at a time of a maximum of the surface mode (g) ($t = 458.6$), and a maximum at the outer boundary (h) ($t = 466.7$). (i) $b_z(x)$ for the same times as in (g) (black) and (h) (orange).

4. Discussion

The analysis of Section 2 together with the simulations in Section 3 have established the theoretical basis for a surface mode at an inner density gradient being excited by driving from an outer boundary. This discussion section aims to tie these results in with the reality of the potential application to large scale plasmapause surface waves, as well as laying out a road map for future studies.

Many previous studies on surface waves consider the limit where the azimuthal wave number is large relative to the field-aligned wave number $\left(k_y/k_z \gg 1\right)$. In this case, the evanescence scale in the direction normal to the surface is inversely proportional to the azimuthal wave number. The wave is then highly confined to the magnetic shells of the surface and the wave frequency depends only on the parallel wave number. The result of this assumption can be seen from Equation A10, giving a surface wave frequency equal to that of an Alfvén mode where the plasma mass density is the mean of the density on each side of the surface (e.g., Southwood & Hughes, 1983; Wentzel, 1979). It is evident that a mode highly confined to near the plasmapause surface is not a candidate for coupling to excitation driven from the magnetopause. Accordingly, we have investigated examples of waves with scale lengths comparable to the scale of the medium in the azimuthal and field-aligned dimensions. The simpler form of the dispersion relation does not then apply. Indeed, Figure A1 shows clearly that there is a significant frequency difference for $k_y \simeq k_z$. The simulation results suggest that for large azimuthal scale sizes of the driving stimulus on the magnetopause, there should be significant penetration to efficiently pump the surface wave at the plasmapause. However, this should be interpreted with caution, as a realistic magnetospheric geometry and Alfvén speed profile, which critically affect the spatial wave properties, would need to be considered to fully make this assertion.

The relative location of the magnetopause and plasmapause is clearly critical to the excitation of a surface wave on the plasmapause. This then ties in to the effect of different prevailing geomagnetic conditions on this mechanism. During periods of heightened activity, with a magnetopause location closer to the Earth, one may expect the separation distance to shorten, therefore increasing the effectiveness of the excitation. However, the structure and location of the plasmapause also vary greatly across different conditions (Carpenter & Anderson, 1992; Goldstein et al., 2019). The width of the plasmapause and the density contrast from the plasmasphere to the plasmatrough are critical parameters that require further investigation for the surface mode excitation. Further, it will be important if comparing to observations that these are appropriately constrained in the data. For example, ensuring accurate ion composition measurements to infer the mass density. These parameters were not varied in our simulations and so changing these will form part of a follow up modeling study. Elsden et al. (2022) showed how the locations of FLRs and the frequencies of waveguide modes varied during different periods of a geomagnetic storm. Small changes in the plasmapause/magnetopause locations had relatively large impacts on the FLR locations, emphasizing how ULF wave properties are very sensitive to the equilibrium. This raises further how plasmapause surface waves relate to the other eigenmodes (cavity/waveguide) of the dayside magnetosphere. For a fixed value of the azimuthal wave number, the surface mode inherently will have a frequency lower than any global mode (e.g., Archer et al., 2022; Kivelson & Southwood, 1986) with the same transverse wave number. It has been beyond the scope of this initial study to properly assess how the surface mode excitation and observability are affected by the presence of other global fast waves. Some evidence is given in Figures 7 and 8 of an inner region cavity mode also being present, but more modeling needs to be done to suggest how this may carry over into a dipolar, inhomogeneous magnetosphere with a realistic Alfvén speed profile.

A recent study by Hartinger et al. (2023) commented on the reasons why the observation of magnetospheric MHD fast “normal modes” (global cavity/waveguide) has been historically difficult. For example, there are often other waves (drift-mirror modes) and transients that can cloud the wave spectra, as well as the fact that they typically do not have a large amplitude compared to say FLRs. The surface waves excited at the plasmapause would be expected to couple to FLRs in the density gradient, as shown in our results, which acts as a very efficient dissipation mechanism. Therefore, it may be that for impulsive or broadband driving, the surface waves are difficult to distinguish clearly in spacecraft observations. It would be interesting to consider observations of FLRs around the plasmapause and whether any of these could be tied to this excitation mechanism. Liu et al. (2011) provide a good example of the difficulty in separating different wave modes in spacecraft data, even with multiple spacecraft on the same orbit. The authors determine that a plasmapause surface wave is a likely candidate to explain $\sim$8mHz oscillations around $L = 5 - 6$ which modulated particle fluxes, though also comment on potential FLR excitation by the surface wave.

There have been several studies in recent years on observations of long period, small azimuthal wavelength surface waves ($m \simeq 36$, He et al., 2020) on the plasmapause, which can result in sawtooth aurora (also known as giant undulations, Henderson et al., 2010; Zhou et al., 2021). These waves have been investigated statistically (Feng et al., 2023), and it is thought they are driven by substorm activity (Hao et al., 2023; Zhou et al., 2024). The MHD instability theory of Viñas and Madden (1986) suggests that a shear flow-ballooning instability can generate low frequency oscillations of the plasmapause boundary. Sorathia et al. (2024) present evidence of giant undulations resulting from such an interchange instability at the plasmapause in global geospace simulations. Horvath and Lovell (2021) observed plasmapause surface waves at the same time as Kelvin-Helmholtz waves on the magnetopause, however the generation mechanism for these surface waves was attributed to undulations of the near-Earth plasma sheet.

While these studies describe oscillations of the plasmapause surface, we believe them to be fundamentally different from the waves proposed in this study in three key ways. First, the azimuthal structure of surface waves relating to giant undulations is usually in the “high-m” regime (short azimuthal wavelength). Our simulations propose a low-m driven surface wave, potentially existing over a substantial MLT range. Indeed, the mechanism proposed here of driving from the magnetopause would not be viable in the high-m limit, as this would cause evanescence of the driving source in the outer magnetosphere, and significant wave power would not reach the plasmapause. Second, the generation mechanism of an interchange instability related to the build up of ring current ions (Sorathia et al., 2024) is completely separate to driving by pressure perturbations at the magnetopause. Third, most of the observations of such high-m plasmapause surface waves are from the dusk flank (Feng et al., 2023; He et al., 2020). This is expected if they are thought to be driven by internal energetic ion injections (Zhou et al., 2024), which have a known dawn-dusk asymmetry (Gabrielse et al., 2014). In our work, we have assumed azimuthal symmetry, and show that in this case, when driving from the dayside, a surface wave would form over a substantial portion of the dayside plasmapause with a low-m azimuthal structure. Introducing azimuthal asymmetry on the dayside (associated with a plasmaspheric plume) should not drastically affect the penetration of a surface wave from the magnetopause to drive the plasmapause surface wave in question (Archer et al., 2023). However, an interesting follow up study would be to consider the ability of the deformed section of the plasmapause during a plume event to support surface waves driven from the magnetopause.

For future observational studies, it is important to provide clear observational criteria for plasmapause surface waves based on our modeling.

1. Radial velocity u_x (or equally azimuthal electric field E_y) will be 90° out of phase with the field-aligned magnetic field perturbation b_z. This follows directly from Equation 9 and holds across all of the simulations in this study (not shown).
2. There should be a peak in the amplitude of b_z, u_x (E_y) across the surface. However, how isolated this peak is will depend heavily on the azimuthal wavenumber (compare the radial profile of b_z between Figures 4a and 5a).
3. An FLR will be excited in the density gradient (plasmapause), though if the gradient is very steep the FLR amplitude may be small (Elsden & Southwood, 2023). Therefore the phase of the azimuthal components (u_y, b_y, E_x) will vary sharply across the plasmapause by 180°.
4. The surface wave should exist over a substantial MLT range (on the dayside for magnetopause driven events).

A good description of previous works relating to plasmapause surface waves is found in the review of Pi2 models by Keiling and Takahashi (2011). This mostly relates to the large azimuthal wavenumber (high-m) case, particularly in relation to previous theory. The situation most often envisaged is that of an impulsive night-side source (e.g., an Earthward bursty bulk flow) impinging upon the plasmapause, driving surface waves. In this context, the plasmapause surface wave has been posited as a candidate to explain large amplitude Pi2 waves at lower latitudes than those observed at the auroral oval (Sutcliffe, 1975). However, plasmaspheric cavity modes (Lester & Orr, 1983) and FLRs (Fukunishi, 1975) provide competing explanations for specific observations. The modeling in this paper could very easily be applied to the nightside excitation of Pi2 waves. There will always be a difficulty in distinguishing between cavity modes and surface waves, particularly with sparse observations. Plasmaspheric cavity modes are radially standing fast waves trapped between the low latitude ionosphere and the plasmapause, whose frequency depends on the geometry of this "cavity" (Keiling & Takahashi, 2011). Both surface waves and cavity modes will have the 90° phase difference between u_x (E_y) and b_z as per point 1 above. Therefore the distinguishing factor will either be found through frequency arguments, or being able to find nodes (zeros) of the cavity mode standing structure which would not be present for a surface wave decaying radially away from the plasmapause. In the broadband simulations presented in this study, there does appear to be some evidence of excitation of a cavity mode of the inner (plasmaspheric) cavity (see Figures 7f and 8f) at higher frequencies than the surface mode. However, the radial mode structure is convoluted by there also being the surface wave present. This relates back to the problem of separating competing fast waves in the data.

Continuing with Pi2 ULF waves, Turner et al. (2015) showed that energetic particles (tens to hundreds of keV) injected during a substorm, were able to reach very low L values ($L < 4$), likely due to their interaction with Pi2 modes. The interpretation was that such waves are plasmaspheric cavity modes, however, as per the above discussion, the phase relations presented are consistent with those in this study, taken from inside the plasmasphere (i.e., inner higher density region) in the evanescent plasmapause surface wave tail (not shown). The purpose of our study was to prove analytically and numerically, that the plasmapause can support a surface wave driven by an external source. Studies like that of Turner et al. (2015) provide a clear avenue for future research, to compare our observational criteria with past and current observations on the dayside and nightside.

A related point to the above but on the dayside, is how ULF can access the inner magnetosphere to meaningfully affect the radiation belts. Rae et al. (2019) show that during geomagnetic storms, an enhanced ring current causes a drop in the Alfvén continuum. This moves the turning point for propagating fast waves further in to the magnetosphere, allowing ULF waves to more easily reach lower L-shells. The excitation of surface waves at the plasmapause gives another mechanism by which significant ULF wave power can access the inner magnetosphere. Furthermore, these fast waves carry an azimuthal electric field component (radial velocity) extended over several L about the surface, dependent on the radial decay length. Evidence of this is given in panels (c) and (f) of Figure 4. This makes these waves a good candidate for drift-resonance with orbiting radiation belt particles. In the situation pictured by Rae et al. (2019), the improved penetration of ULF waves from the magnetopause during storms would also provide the driving stimulus envisaged in our study, to seed the excitation of the plasmapause surface wave. Further, this could help to explain previous observations of "non-FLRs" (i.e., fast modes) further away from auroral latitudes (Baker et al., 2003).

5. Conclusions

The main findings of this study can be summarized as follows:

1. An analytical form for a surface wave at a density gradient (e.g., plasmapause), driven from an outer boundary (e.g., magnetopause) is derived in the MHD box model.
2. The frequency of such surface waves is found to be almost identical to the classical surface wave frequency, when the driven outer boundary is placed sufficiently far away from the surface.
3. These findings are corroborated by MHD simulations, which show how a surface wave on the plasmapause can be excited through a variety of driving stimuli on the magnetopause boundary (monochromatic, impulsive, continuous broadband).
4. This provides a mechanism by which ULF waves can access the inner magnetosphere, important for wave-particle interactions in the radiation belts.
5. The azimuthal scale size of these waves is envisaged to be large, separating this wave from smaller scale plasmapause surface waves driven on the dusk-side plasmapause during storms and substorms.
6. Follow up studies will investigate a dipole magnetic field geometry and different radial Alfvén speed profiles, representing a variety of geomagnetic conditions.

Appendix A: Derivation of Surface Mode Frequency Following Wentzel (1979)

In this appendix, we expand on some of the derivations of Wentzel (1979) and provide an exact analytical form for the frequency in the case of the surface wave decaying to zero on both sides of the surface (i.e., without the driven boundary condition). Wentzel (1979) only provides a formula depending on particular limits of the ratio of the wavenumbers k_y/k_z. We further compare this to the workings of Uberoi (1989), who also provide an analytical solution for the frequency. We have included these workings in detail as a hope of clarifying the procedure for future readers, which appears in different forms across previous works.

The starting point is Equations 4–7 from Section 2, which are reproduced below for ease of reading:

$$b_{z1} = C_1 e^{K_1 x} + D_1 e^{-K_1 x}, \tag{A1}$$

$$b_{z2} = C_2 e^{K_2 x} + D_2 e^{-K_2 x}, \tag{A2}$$

where

$$K_1 = \sqrt{k_y^2 - \frac{\epsilon_1}{B_0^2}}, \tag{A3}$$

$$K_2 = \sqrt{k_y^2 - \frac{\epsilon_2}{B_0^2}}, \tag{A4}$$

and the density surface is at $x = 0$. For boundary conditions, we drop the outer driven boundary condition and require that $b_z \to 0$ as $|x| \to \infty$. Hence we are considering the natural frequency of the surface wave. Therefore in region 1, for $x < 0$, this implies that $D_1 = 0$. Similarly in region 2 for $x > 0$, $C_2 = 0$. At the surface $x = 0$, we require continuity of b_z and normal displacement ξ_x that is, at $x = 0$

$$b_{z1} = b_{z2},$$
$$\Rightarrow C_1 = D_2 = A.$$

Using Equation 9 we can write the condition for normal displacement in terms of the derivative of b_z as

$$\xi_{x1}|_{x=0^-} = \xi_{x2}|_{x=0^+},$$
$$\frac{1}{\epsilon_1}\frac{\mathrm{d}b_{z1}}{\mathrm{d}x}|_{x=0^-} = \frac{1}{\epsilon_2}\frac{\mathrm{d}b_{z2}}{\mathrm{d}x}|_{x=0^+}, \tag{A5}$$

where the derivatives are simply calculated from Equations A1 and A2 as

$$\frac{\mathrm{d}b_{z1}}{\mathrm{d}x} = AK_1 e^{K_1 x},$$
$$\frac{\mathrm{d}b_{z2}}{\mathrm{d}x} = -AK_2 e^{-K_2 x}.$$

Then Equation A5 gives

$$\frac{K_1}{\epsilon_1} + \frac{K_2}{\epsilon_2} = 0, \tag{A6}$$

which is Equation 9 from Uberoi (1989). Following Wentzel (1979), squaring Equation A6 gives the condition

$$\frac{K_1^2}{\epsilon_1^2} = \frac{K_2^2}{\epsilon_2^2}, \tag{A7}$$

requiring the negative root solution to satisfy Equation A6 (Equation 10; Wentzel, 1979). Rewriting Equation A7 as

$$K_1^2 = r^2 K_2^2, \tag{A8}$$

with $r = \epsilon_1/\epsilon_2$ and requiring $r < 0$ to satisfy the negative root condition, we can rearrange this equation involving r to get

$$\begin{aligned} r &= \frac{\epsilon_1}{\epsilon_2} = \frac{\mu_0\rho_1\omega^2 - k_z^2 B_0^2}{\mu_0\rho_2\omega^2 - k_z^2 B_0^2}, \\ \left(\mu_0\rho_2\omega^2 - k_z^2 B_0^2\right) r &= \mu_0\rho_1\omega^2 - k_z^2 B_0^2, \\ \frac{\omega^2}{k_z^2} &= \frac{B_0^2(r-1)}{\mu_0\rho_2 r - \mu_0\rho_1}, \\ \frac{\omega^2}{k_z^2} &= \frac{B_0^2(1-r)}{\mu_0\left(\rho_1 - \rho_2 r\right)}. \end{aligned} \tag{A9}$$

Hence, Equation A9 gives the frequency as a function of the parameter r, however r itself depends on ω through ϵ_1, ϵ_2. Various arguments are often made to set $r = -1$, which then yields

$$\omega^2 = \frac{2k_z^2 B_0^2}{\mu_0\left(\rho_1 + \rho_2\right)}. \tag{A10}$$

For example, Wentzel (1979) shows that this holds under the assumption of an incompressible medium or for small k_z/k_y (hence large k_y/k_z). However, we can solve generally for ω without assuming a value for r. Begin by rewriting ϵ_2 in terms of the frequency in Equation A9 as

10.1029/2025JA033830

$$
\begin{aligned}
\epsilon_2 &= \mu_0\rho_2\omega^2 - k_z^2B_0^2,\\
\epsilon_2 &= \rho_2\left(\frac{k_z^2B_0^2(1-r)}{\rho_1 - r\rho_2}\right) - k_z^2B_0^2,\\
\frac{\epsilon_2}{B_0^2} &= \frac{k_z^2\left(\rho_2(1-r) - (\rho_1 - r\rho_2)\right)}{\rho_1 - r\rho_2},\\
\frac{\epsilon_2}{B_0^2} &= k_z^2\left(\frac{\rho_2 - \rho_1}{\rho_1 - r\rho_2}\right).
\end{aligned} \tag{A11}
$$

This is Equation 16 of Wentzel (1979). It now falls to determine the values that r can take. Define a variable Q, using Equation A11 as

$$
Q = \frac{k_y^2B_0^2}{\epsilon_2} = \frac{k_y^2}{k_z^2}\frac{\rho_1 - r\rho_2}{\rho_2 - \rho_1}. \tag{A12}
$$

Notice from Equation A4 that

$$
\begin{aligned}
K_2^2 &= k_y^2 - \frac{\epsilon_2}{B_0^2},\\
&= k_y^2\left(1 - \frac{\epsilon_2}{k_y^2B_0^2}\right),\\
&= k_y^2\left(1 - \frac{1}{Q}\right).
\end{aligned} \tag{A13}
$$

Then replace ϵ_1 in the form for K_1 (Equation A3) using $r = \epsilon_1/\epsilon_2$:

$$
\begin{aligned}
K_1^2 &= k_y^2 - \frac{\epsilon_1}{B_0^2},\\
&= k_y^2 - \frac{r\epsilon_2}{B_0^2},\\
&= k_y^2\left(1 - \frac{r\epsilon_2}{k_y^2B_0^2}\right),\\
&= k_y^2\left(1 - \frac{r}{Q}\right).
\end{aligned} \tag{A14}
$$

Then using Equations A13 and A14 in Equation A8 gives:

$$
K_1^2 = r^2K_2^2, \tag{A15}
$$

$$
k_y^2\left(1 - \frac{r}{Q}\right) = r^2k_y^2\left(1 - \frac{1}{Q}\right), \tag{A16}
$$

$$
r^2(Q-1) + r - Q = 0, \tag{A17}
$$

which is Equation 18 of Wentzel (1979). Solving the quadratic in r gives

$$
\begin{aligned}
r &= \frac{-1 \pm \sqrt{1 + 4(Q-1)Q}}{2(Q-1)},\\
r &= -\frac{Q}{Q-1},
\end{aligned} \tag{A18}
$$

where the negative root is chosen to enforce that r is negative, as required. It can be seen that for large Q (which corresponds to large k_y/k_z from Equation A12), $r \rightarrow -1$. Equation A18 is an expression for r as a function of Q, while Equation A12 gives Q as a function of r. Hence, one can be eliminated in favor of the other to ultimately determine ω. Choosing to eliminate r using Equation A18 in the expression for Q, Equation A12, gives

$$\begin{aligned}
Q &= \frac{k_y^2}{k_z^2}\frac{\rho_1 - r\rho_2}{\rho_2 - \rho_1}, \\
Q &= \frac{k_y^2}{k_z^2}\frac{\rho_1 + \rho_2 \frac{Q}{Q-1}}{\rho_2 - \rho_1}, \\
(\rho_2 - \rho_1)(Q-1)Q &= \frac{k_y^2}{k_z^2}(\rho_1(Q-1) + Q\rho_2), \\
(Q^2 - Q)(\rho_2 - \rho_1) &= \frac{k_y^2}{k_z^2}\rho_1(Q-1) + \frac{k_y^2}{k_z^2}Q\rho_2, \\
Q^2(\rho_2 - \rho_1) - Q\left(\rho_2 - \rho_1 + \frac{k_y^2}{k_z^2}(\rho_1 + \rho_2)\right) + \frac{k_y^2}{k_z^2}\rho_1 &= 0.
\end{aligned}$$

Solving this quadratic for Q then gives

$$Q = \frac{1}{2(\rho_2 - \rho_1)}\left\{\left(\rho_2 - \rho_1 + \frac{k_y^2}{k_z^2}(\rho_1 + \rho_2)\right) \pm \sqrt{\left(\rho_2 - \rho_1 + \frac{k_y^2}{k_z^2}(\rho_1 + \rho_2)\right)^2 - 4\frac{k_y^2}{k_z^2}(\rho_2 - \rho_1)\rho_1}\right\}. \tag{A19}$$

The sign of Q is set by which region is set to have a lower density. This is clear from Equation A12, where given $r < 0$ and assuming $\rho_2 < \rho_1$, then Q is negative. It can be seen that Q is of the form

$$Q = a\left(X \pm \sqrt{X^2 + b}\right),$$

with a negative and b positive (again since $(\rho_2 - \rho_1) < 0$ by definition), hence the positive root must be taken in Equation A12 to ensure Q is negative. The term under the square root can be rewritten as

$$\begin{aligned}
&\left(\rho_2 - \rho_1 + \frac{k_y^2}{k_z^2}(\rho_1 + \rho_2)\right)^2 - 4\frac{k_y^2}{k_z^2}(\rho_2 - \rho_1)\rho_1 \\
&= (\rho_2 - \rho_1)^2\left(\left(1 + \frac{k_y^2}{k_z^2}\frac{(\rho_1 + \rho_2)}{(\rho_2 - \rho_1)}\right)^2 - 4\frac{k_y^2}{k_z^2}\frac{\rho_1}{\rho_2 - \rho_1}\right).
\end{aligned}$$

All together, this then allows Q to be given by

$$Q = \frac{1}{2}\left\{1 + \frac{k_y^2}{k_z^2}\frac{(\rho_1 + \rho_2)}{(\rho_2 - \rho_1)} - \sqrt{\left(1 + \frac{k_y^2}{k_z^2}\frac{(\rho_1 + \rho_2)}{(\rho_2 - \rho_1)}\right)^2 - 4\frac{k_y^2}{k_z^2}\frac{\rho_1}{\rho_2 - \rho_1}}\right\}, \tag{A20}$$

where the minus sign now in front of the square root is again enforced by Q being negative, and can be seen as being introduced when choosing to take the factor of $(\rho_2 - \rho_1)^2$ out from the square root. Hence, Q is determined purely in terms of the wavenumbers k_y, k_z and the densities ρ_1, ρ_2. Thus r is found from Equation A18, which then determines the frequency ω from Equation A9.

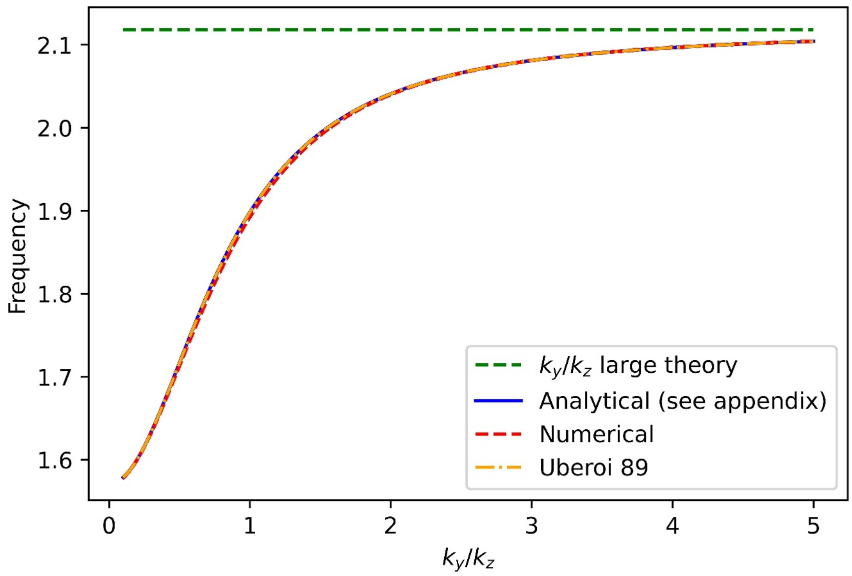

Figure A1. Surface mode frequency, ω, against the wavenumber ratio k_y/k_z calculated by different methods. The blue line gives the analytic formula from this appendix. The dot-dash orange line follows the solution of Uberoi (1989). The red dashed line is derived by finding which frequency maximizes the amplitude at the surface using the analytic form for b_z from Equation 19, assuming a driven boundary condition. The green dashed line uses the large k_y/k_z approximation from Equation A10.

Figure A1 displays the frequency ω against the ratio of the wavenumbers k_y/k_z, calculated in several different ways, for the densities $\rho_1 = 1$ and $\rho_2 = 0.1$, and assuming $k_z = \pi/2$. The solid blue line uses the method outlined in this appendix to find ω analytically. The dashed red line uses the analytical form for b_z found in Equation 19 in Section 2, and searches for the frequency which maximizes the amplitude at the surface (method discussed further in the main text). To evaluate Equation 19, a location of the driven boundary (x_m) must be specified. It turns out that when this value is taken close to the density surface, it changes the frequency which maximizes the surface mode amplitude. In the example shown, it is set as $x_m = 1$ (for a surface at $x = 0$) and one can see that the dashed red line sits below the others for intermediate k_y/k_z. Setting $x_m = 3$ makes the lines indistinguishable (not shown here), so clearly as the driven boundary is moved further away from the surface, the frequencies agree more closely. However, it does indeed show that the addition of a driven boundary creates a different frequency of surface wave, albeit only slightly in this case.

The dashed green line represents the limit of taking $r = -1$, resulting in Equation A10 for the frequency. This clearly becomes more accurate when k_y/k_z increases, as expected from the previous theory (Wentzel, 1979). This emphasizes the importance of using the full solution for intermediate values of k_y/k_z. A similar plot was produced by Uberoi (1989), so their method was also investigated. Their solution (through solving their Equation 13) is plotted as the dashed orange line, which is in exact agreement with our approach. This was a useful check to show agreement between the theories.

We can further show how the natural surface frequency ω varies for different density ratios. This is shown in Figure A2 and provides a better understanding of the solution space, where the solutions are found as detailed previously in this appendix, again assuming $k_z = \pi/2$. It can be seen that changing the density ratio substantially

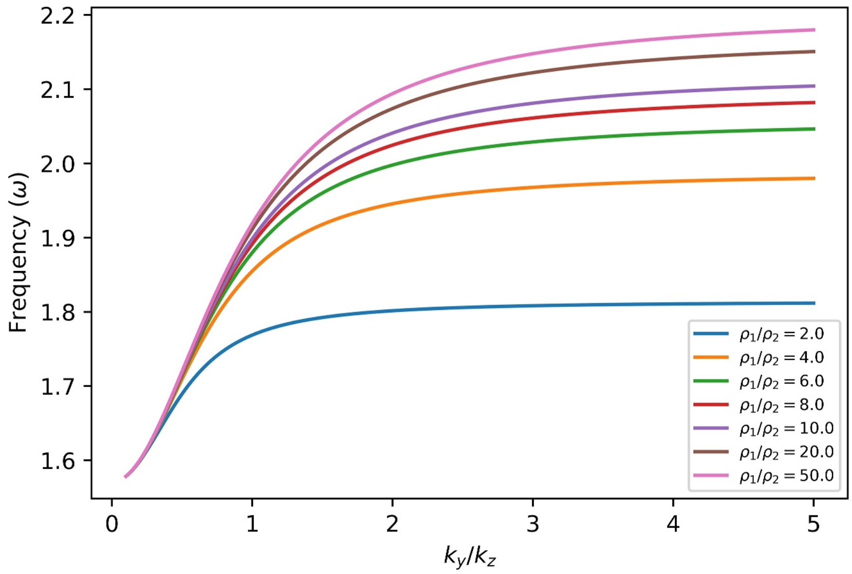

Figure A2. Surface mode frequency, ω, against the wavenumber ratio k_y/k_z for different density ratios ρ_1/ρ_2. The ratio of $\rho_1/\rho_2 = 10$ (purple line) is that used in Figure A1.

changes the resulting frequency. This figure could be used as a guide of the expected plasmapause surface wave frequency, if plasma density measurements were taken either side of the plasmapause.

Data Availability Statement

The data used to produce the figures in this manuscript can be found at https://doi.org/10.6084/m9.figshare.28369787.v2 (Elsden, 2025).

Acknowledgments
This research was supported by the International Space Science Institute (ISSI) in Bern, through ISSI International Team project #546 "Magnetohydrodynamic Surface Waves at Earth's Magnetosphere (and Beyond)." MOA was supported by UKRI (STFC/EPSRC) Stephen Hawking Fellowship EP/T01735X/1 and UKRI Future Leaders Fellowship MR/X034704/1. MDH was supported by NASA Grant 80NSSC21K1677. OA would like to acknowledge financial support from the University of Birmingham, the University of Exeter, and also from the United Kingdom Research and Innovation (UKRI) Natural Environment Research Council (NERC) Independent Research Fellowship NE/V013963/1 and NE/V013963/2. ANW was partially funded by the Science and Technology Facilities Council (STFC) Grant (ST/N000609/1).

References

Archer, M. O., Hartinger, M. D., Plaschke, F., Southwood, D. J., & Rastaetter, L. (2021). Magnetopause ripples going against the flow form azimuthally stationary surface waves. *Nature Communications*, *12*(1), 5697. https://doi.org/10.1038/s41467-021-25923-7

Archer, M. O., Pilipenko, V. A., Li, B., Sorathia, K., Nakariakov, V. M., Elsden, T., & Nykyri, K. (2024). Magnetopause MHD surface wave theory: Progress & challenges. *Frontiers in Astronomy and Space Sciences*, *11*, 1407172. https://doi.org/10.3389/fspas.2024.1407172

Archer, M. O., & Plaschke, F. (2015). What frequencies of standing surface waves can the subsolar magnetopause support? *Journal of Geophysical Research: Space Physics*, *120*(5), 3632–3646. https://doi.org/10.1002/2014JA020545

Archer, M. O., Southwood, D. J., Hartinger, M. D., Rastaetter, L., & Wright, A. N. (2022). How a realistic magnetosphere alters the polarizations of surface, fast magnetosonic, and Alfven waves. *Journal of Geophysical Research: Space Physics*, *127*(2), e2021JA030032. https://doi.org/10.1029/2021JA030032

Archer, M. O., Southwood, D. J., Hartinger, M. D., Rastätter, L., & Nykyri, K. (2023). Magnetosonic ULF waves with anomalous plasma–magnetic field correlations: Standing waves and inhomogeneous plasmas. *Geophysical Research Letters*, *50*(16), e2023GL104762. https://doi.org/10.1029/2023GL104762

Baker, G. J., Donovan, E. F., & Jackel, B. J. (2003). A comprehensive survey of auroral latitude PC5 pulsation characteristics. *Journal of Geophysical Research*, *108*(A10), 1384. https://doi.org/10.1029/2002JA009801

Carpenter, D. L., & Anderson, R. R. (1992). An ISEE/whistler model of equatorial electron density in the magnetosphere. *Journal of Geophysical Research*, *97*(A2), 1097–1108. https://doi.org/10.1029/91JA01548

Chen, L., & Hasegawa, A. (1974). A theory of long-period magnetic pulsations: 2. Impulse excitation of surface eigenmode. *Journal of Geophysical Research*, *79*(7), 1033–1037. https://doi.org/10.1029/JA079i007p01033

Del Corpo, A., Vellante, M., Heilig, B., Pietropaolo, E., Reda, J., & Lichtenberger, J. (2020). An empirical model for the dayside magnetospheric plasma mass density derived from EMMA magnetometer network observations. *Journal of Geophysical Research: Space Physics*, *125*(2), e2019JA027381. https://doi.org/10.1029/2019JA027381

Di Matteo, S., Villante, U., Viall, N., Kepko, L., & Wallace, S. (2022). On differentiating multiple types of ULF magnetospheric waves in response to solar wind periodic density structures. *Journal of Geophysical Research: Space Physics*, *127*(3), e2021JA030144. https://doi.org/10.1029/2021JA030144

Elsden, T. (2025). Dataset for theory and modelling of large scale plasmapause surface waves [Dataset]. https://doi.org/10.6084/m9.figshare.28369787.v2

Elsden, T., & Southwood, D. J. (2023). Modeling features of field line resonance observable by a single spacecraft at Saturn. *Journal of Geophysical Research (Space Physics)*, *128*(3), e2022JA031208. https://doi.org/10.1029/2022JA031208

Elsden, T., Yeoman, T. K., Wharton, S. J., Rae, I. J., Sandhu, J. K., Walach, M.-T., et al. (2022). Modeling the varying location of field line resonances during geomagnetic storms. *Journal of Geophysical Research: Space Physics*, *127*(1), e2021JA029804. https://doi.org/10.1029/2021JA029804

Feng, Z.-J., Ren, J., Zong, Q.-G., Xiang, T.-Y., & Ai, X.-Y. (2023). Statistical properties of long-period plasmapause surface waves from Van Allen probes observations. *Journal of Geophysical Research: Space Physics*, *128*(7), e2023JA031572. https://doi.org/10.1029/2023JA031572

Fukunishi, H. (1975). Polarization changes of geomagnetic PI 2 pulsations associated with the plasmapause. *Journal of Geophysical Research*, *80*(1), 98–110. https://doi.org/10.1029/JA080i001p00098

Fukunishi, H., & Lanzerotti, L. J. (1974). ULF pulsation evidence of the plasmapause 2. Polarization studies of Pc 3 and Pc 4 pulsations near L=4 and at a latitude network in the conjugate region. *Journal of Geophysical Research*, *79*(31), 4632–4647. https://doi.org/10.1029/JA079i031p04632

Gabrielse, C., Angelopoulos, V., Runov, A., & Turner, D. L. (2014). Statistical characteristics of particle injections throughout the equatorial magnetotail. *Journal of Geophysical Research: Space Physics*, *119*(4), 2512–2535. https://doi.org/10.1002/2013JA019638

Gallagher, D. L., Craven, P. D., & Comfort, R. H. (2000). Global core plasma model. *Journal of Geophysical Research*, *105*(A8), 18819–18833. https://doi.org/10.1029/1999JA000241

Goldstein, J., Pascuale, S., & Kurth, W. S. (2019). Epoch-based model for stormtime plasmapause location. *Journal of Geophysical Research: Space Physics*, *124*(6), 4462–4491. https://doi.org/10.1029/2018JA025996

Hao, Y. X., Zong, Q. G., Yue, C., Zhou, X. Z., Zhang, H., Pu, Z. Y., & Shprits, Y. Y. (2023). Plasmapause surface waves triggered by substorms. *Journal of Geophysical Research (Space Physics)*, *128*(6), e2021JA029962. https://doi.org/10.1029/2021JA029962

Hartinger, M. D., Elsden, T., Archer, M. O., Takahashi, K., Wright, A. N., Artemyev, A., et al. (2023). Properties of magnetohydrodynamic normal modes in the earth's magnetosphere. *Journal of Geophysical Research: Space Physics*, *128*(12), e2023JA031987. https://doi.org/10.1029/2023JA031987

He, F., Guo, R.-L., Dunn, W. R., Yao, Z.-H., Zhang, H.-S., Hao, Y.-X., et al. (2020). Plasmapause surface wave oscillates the magnetosphere and diffuse aurora. *Nature Communications*, *11*(1), 1668. https://doi.org/10.1038/s41467-020-15506-3

Henderson, M. G., Donovan, E. F., Foster, J. C., Mann, I. R., Immel, T. J., Mende, S. B., & Sigwarth, J. B. (2010). Start-to-end global imaging of a sunward propagating, saps-associated giant undulation event. *Journal of Geophysical Research*, *115*(A4), A04210. https://doi.org/10.1029/2009JA014106

Horvath, I., & Lovell, B. C. (2021). Subauroral flow channel structures and auroral undulations triggered by Kelvin-Helmholtz waves. *Journal of Geophysical Research: Space Physics*, *126*(6), e2021JA029144. https://doi.org/10.1029/2021JA029144

Keiling, A., & Takahashi, K. (2011). Review of Pi2 models. *Space Science Reviews*, *161*(1–4), 63–148. https://doi.org/10.1007/s11214-011-9818-4

Kivelson, M. G., & Southwood, D. J. (1986). Coupling of global magnetospheric MHD eigenmodes to field line resonances. *Journal of Geophysical Research*, *91*(A4), 4345–4351. https://doi.org/10.1029/JA091iA04p04345

Lanzerotti, L. J., Fukunishi, H., Hasegawa, A., & Chen, L. (1973). Excitation of the plasmapause at ultralow frequencies. *Physical Review Letters*, *31*(10), 624–628. https://doi.org/10.1103/PhysRevLett.31.624

Lemaire, J. F. (1974). The 'roche-limit' of ionospheric plasma and the formation of the plasmapause. *Planetary and Space Science*, *22*(5), 757–766. https://doi.org/10.1016/0032-0633(74)90145-7

Lemaire, J. F., & Gringauz, K. I. (1998). *The Earth's plasmasphere*. Cambridge University Press.

Lester, M., & Orr, D. (1983). Correlations between ground observations of Pi 2 geomagnetic pulsations and satellite plasma density observations. *Planetary and Space Science*, *31*(2), 143–160. https://doi.org/10.1016/0032-0633(83)90050-8

Liu, W., Sarris, T. E., Li, X., Zong, Q.-G., Ergun, R., Angelopoulos, V., & Glassmeier, K. H. (2011). Spatial structure and temporal evolution of a dayside poloidal ULF wave event. *Geophysical Research Letters*, *38*(19), L19104. https://doi.org/10.1029/2011GL049476

Nakariakov, V. M., Pilipenko, V., Heilig, B., Jelínek, P., Karlický, M., Klimushkin, D. Y., et al. (2016). Magnetohydrodynamic oscillations in the solar Corona and earth's magnetosphere: Towards consolidated understanding. *Space Science Reviews*, *200*(1–4), 75–203. https://doi.org/10.1007/s11214-015-0233-0

Nenovski, P. (2021). MHD surface waves - A source of global magnetospheric modes (resonances)? *Advances in Space Research*, *67*(2), 731–738. https://doi.org/10.1016/j.asr.2020.09.039

Nenovski, P., Villante, U., Francia, P., Vellante, M., & Bochev, A. (2007). Do we need a surface wave approach to the magnetospheric resonances? *Planetary and Space Science*, *55*(6), 680–693. https://doi.org/10.1016/j.pss.2006.04.038

Plaschke, F., & Glassmeier, K. H. (2011). Properties of standing Kruskal-Schwarzschild-modes at the magnetopause. *Annales Geophysicae*, *29*(10), 1793–1807. https://doi.org/10.5194/angeo-29-1793-2011

Plaschke, F., Glassmeier, K.-H., Auster, H. U., Constantinescu, O. D., Magnes, W., Angelopoulos, V., et al. (2009). Standing Alfvén waves at the magnetopause. *Geophysical Research Letters*, *36*(2), L02104. https://doi.org/10.1029/2008GL036411

Plaschke, F., Hietala, H., Archer, M., Blanco-Cano, X., Kajdič, P., Karlsson, T., et al. (2018). Jets downstream of collisionless shocks. *Space Science Reviews*, *214*(5), 81. https://doi.org/10.1007/s11214-018-0516-3

Poedts, S., Goossens, M., & Kerner, W. (1989). Numerical simulation of coronal heating by resonant absorption of Alfvén waves. *Solar Physics*, *123*(1), 83–115. https://doi.org/10.1007/BF00150014

Rae, I. J., Murphy, K. R., Watt, C. E. J., Sandhu, J. K., Georgiou, M., Degeling, A. W., et al. (2019). How do ultra-low frequency waves access the inner magnetosphere during geomagnetic storms? *Geophysical Research Letters*, *46*(19), 10699–10709. https://doi.org/10.1029/2019GL082395

Ripoll, J.-F., Thaller, S. A., Hartley, D. P., Cunningham, G. S., Pierrard, V., Kurth, W. S., et al. (2022). Statistics and empirical models of the plasmasphere boundaries from the Van Allen probes for radiation belt physics. *Geophysical Research Letters*, *49*(21), e2022GL101402. https://doi.org/10.1029/2022GL101402

Sorathia, K. A., Shumko, M., Sciola, A., Michael, A., Merkin, V. G., Gallardo-Lacourt, B., et al. (2024). Identifying the magnetospheric drivers of giant undulations: Global modeling of the evolving inner magnetosphere and its auroral manifestations. *Geophysical Research Letters*, *51*(16), e2024GL110772. https://doi.org/10.1029/2024GL110772

Southwood, D. J. (1974). Some features of field line resonances in the magnetosphere. *Planetary and Space Science*, *22*(3), 483–491. https://doi.org/10.1016/0032-0633(74)90078-6

Southwood, D. J., & Hughes, W. J. (1983). Theory of hydromagnetic waves in the magnetosphere. *Space Science Reviews*, *35*(4), 301–366. https://doi.org/10.1007/BF00169231

Sutcliffe, P. R. (1975). The association of harmonics in Pi2 power spectra with the plasmapause. *Planetary and Space Science*, *23*(12), 1581–1587. https://doi.org/10.1016/0032-0633(75)90085-9

Takahashi, K., & Ukhorskiy, A. Y. (2007). Solar wind control of Pc5 pulsation power at geosynchronous orbit. *Journal of Geophysical Research (Space Physics)*, *112*(A11), 11205. https://doi.org/10.1029/2007JA012483

Turner, D. L., Claudepierre, S. G., Fennell, J. F., O'Brien, T. P., Blake, J. B., Lemon, C., et al. (2015). Energetic electron injections deep into the inner magnetosphere associated with substorm activity. *Geophysical Research Letters*, *42*(7), 2079–2087. https://doi.org/10.1002/2015GL063225

Uberoi, C. (1989). Resonant absorption of Alfvén compressional surface waves. *Journal of Geeophysical Research*, *94*(A6), 6941–6944. https://doi.org/10.1029/JA094iA06p06941

Viñas, A. F., & Madden, T. R. (1986). Shear flow-ballooning instability as a possible mechanism for hydromagnetic fluctuations. *Journal of Geophysical Research*, *91*(A2), 1519–1528. https://doi.org/10.1029/JA091iA02p01519

Wentzel, D. G. (1979). Hydromagnetic surface waves. *Astrophysical Journal*, *227*, 319–322. https://doi.org/10.1086/156732

Wright, A. N. (1994). Dispersion and wave coupling in inhomogeneous MHD waveguides. *Journal of Geophysical Research*, *99*(A1), 159–167. https://doi.org/10.1029/93JA02206

Wright, A. N., & Elsden, T. (2020). Simulations of MHD wave propagation and coupling in a 3-D magnetosphere. *Journal of Geophysical Research (Space Physics)*, *125*(2), e27589. https://doi.org/10.1029/2019JA027589

Wright, A. N., & Rickard, G. J. (1995). A numerical study of resonant absorption in a magnetohydrodynamic cavity driven by a broadband spectrum. *Astrophysical Journal*, *444*, 458–470. https://doi.org/10.1086/175620

Wright, A. N., & Thompson, M. J. (1994). Analytical treatment of Alfvén resonances and singularities in nonuniform magnetoplasmas. *Physics of Plasmas*, *1*(3), 691–705. https://doi.org/10.1063/1.870815

Zhou, Y.-J., He, F., Archer, M. O., Zhang, X.-X., Hao, Y. X., Yao, Z.-H., et al. (2024). Spatial evolution characteristics of plasmapause surface wave during a geomagnetic storm on 16 July 2017. *Geophysical Research Letters*, *51*(8), e2024GL109371. https://doi.org/10.1029/2024GL109371

Zhou, Y.-J., He, F., Zhang, X.-X., Yao, Z.-H., Wei, Y., & Zhang, Y.-L. (2021). Statistical characteristics of giant undulations during geomagnetic storms. *Geophysical Research Letters*, *48*(13), e93098. https://doi.org/10.1029/2021GL093098